A wireless, portable triboelectric spirometer for point-of-care pulmonary function monitoring

Qinghao Xu[1,6], Yunsheng Fang[2,6], Qingshen Jing[3,6], Ning Hu[1,6], Nicole Ke Lin[2], Yifan Pan[4], Lin Xu[5], Haiqi Gao[1], Ming Yuan[1], Liang Chu[1], Yanwen Ma[1], Yannan Xie[1*], Jun Chen[2*]& Lianhui Wang[1*]

[1]Key Laboratory for Organic Electronics and Information Displays & Institute of Advanced Materials, Jiangsu Key Laboratory for Biosensors, Jiangsu National Synergetic Innovation Center for Advanced Materials, Nanjing University of Posts and Telecommunications, Nanjing, Jiangsu 210023, China.

[2]Department of Bioengineering, University of California, Los Angeles, Los Angeles, California 90095, USA.

[3]Department of Materials Science and Metallurgy, University of Cambridge, Cambridge CB2 1TN, UK.

[4]Viterbi School of Engineering, University of Southern California, Los Angeles, California 90007, USA.

[5]Jiangsu Key Laboratory of New Power Batteries, Collaborative Innovation Center of Biomedical Functional Materials, School of Chemistry and Materials Science, Nanjing Normal University, Nanjing, Jiangsu 210023, China.

[6]These authors contributed equally to this work.

*Corresponding email: iamynxie@njupt.edu.cn(Y.X.);

jun.chen@ucla.edu(J.C.);

iamlhwang@njupt.edu.cn (L.W.)

Abstract

Coronavirus disease 2019 (COVID-19) as a severe acute respiratory syndrome infection has spread rapidly across the world since its emergence in 2019 and drastically altered our way of life. Patients who have recovered from COVID-19 may still face persisting respiratory damage from the virus, necessitating long-term supervision after discharge to closely assess pulmonary function during rehabilitation. Therefore, developing portable spirometers for pulmonary function tests is of great significance for convenient home-based monitoring during recovery. Here, we propose a wireless, portable pulmonary function monitor for rehabilitation care after COVID-19. It is composed of a breath-to-electrical (BTE) sensor, a signal processing circuit, and a Bluetooth communication unit. The BTE sensor, with a compact size and light weight of 2.5 cm^3 and 1.8 g respectively, is capable of converting respiratory biomechanical motions into considerable electrical signals. The output signal stability is greater than 93% under 35%-81% humidity, which allows for ideal expiration airflow sensing. Through a wireless communication circuit system, the signals can be received by a mobile terminal and processed into important physiological parameters, such as forced expiratory volume in one second (FEV_1) and forced vital capacity (FVC). The FEV_1/FVC ratio, is then calculated to further evaluate pulmonary function of testers. Through these measurement methods, the acquired pulmonary function parameters are shown to exhibit high accuracy (>97%) in comparison to a commercial spirometer. The practical design of the self-powered flow spirometer presents a low-cost and convenient method for pulmonary function monitoring during rehabilitation from COVID-19.

Keywords: COVID-19, self-powered sensors, triboelectric nanogenerators, spirometers, pulmonary function tests

1. Introduction

Within merely one year, coronavirus disease 2019 (COVID-19), an infectious disease with potential for severe lung damage (Fig. 1A), has infected tens of millions of people worldwide and killed millions of others (Zhao et al., 2020; Fajnzylber et al., 2020). To date, COVID-19 has not yet been effectively treated, and the pulmonary function of surviving patients still requires long-term monitoring after discharge (You et al., 2020). Pulmonary function tests (PFTs) based on spirometry are noninvasive diagnostic tools that monitor lung function through recording volume-flow curves of respiration, thereby providing critical pulmonary function parameters (Dirksen et al., 1998), such as forced expiratory volume in one second (FEV_1) and forced vital capacity (FVC). It has been reported that both FEV_1 and FVC values are generally smaller than the lower normality values in discharged COVID-19 patients, whereas FEV_1/FVC is above the upper limit of normality values at the initial stage of clinical recovery (Fumagalli et al., 2020). During the rehabilitation period, the above indicators will return to normal, with both the FEV_1 and FVC increasing as their ratio decreases. Therefore, the spirometer is an important instrument recommended for daily wear that monitors and evaluates pulmonary function for rehabilitation care after COVID-19 (Chung et al., 2019). Conventional spirometry facilities are typically restricted to hospitals, and the growing number of COVID-19 patients may potentially cause extreme shortages of medical supplies. In fact, many hospitals are now no longer providing PFT services due to pandemic-related risks, in order to reduce cross-infection rates (Kouri et al., 2020). Moreover, requiring patients to regularly visit the hospital during lockdown is

particularly inconvenient and may contribute to growing infection rates as well. An ideal approach would be to develop innovative and cost-effective point-of-care testing instruments featuring portable and wireless systems, through which discharged patients can self-test at home while their physiological signals are transmitted to mobile terminals and monitored on the cloud by physicians (Fig. 1B).

Conventional spirometers are categorized into volume-measurement and flow-measurement types (Graham et al., 2019; Leocadio et al., 2019). Compared to volume spirometers, flow spirometers are more compact, allowing for better adaptability to any minimization of test instruments. Typically, various sensors are employed to monitor the velocity of airflow and integrate the volume over time. These sensors are generally classified into four categories according to their individualized working mechanisms: differential pressure pneumotachometers, hot wire anemometers, rotating vane spirometers, and ultrasonic flowmeters (Zhou et al., 2019). However, the wide-range adoption of these spirometers has been overshadowed by the following limitations. Firstly, because these large devices require frequent maintenance, they are typically only available in hospitals and therefore inaccessible for the home-quarantined patient during the COVID-19 pandemic. Moreover, using the same equipment to take measurements of different patients inherently possesses a large probability for cross-infection. Even if commercial home-based instruments are used instead, they are expensive due to their sophisticated structures and mechanisms (West and Theron, 2015), which largely increases the financial burden for COVID-19 patients. In this regard, developing a portable and low-cost spirometer based on novel sensing

principles is imperative for pulmonary function monitoring during recovery from COVID-19.

Self-powered sensors based on emerging triboelectric nanogenerator technology have been demonstrated to possess promising sensing capabilities with numerous advantages, such as simple structure, high robustness, and low cost (Fan et al., 2012; Wang, 2014; Pu et al., 2017; Guo et al., 2018; Lu et al., 2019). Such sensors are capable of generating significant electrical signals in response to ambient stimuli without external power supply. Moreover, their output signals can be directly used as sensing signals to reflect the dynamic changes of their sensing elements (Wang et al., 2015; Su et al., 2020; Jiang et al., 2020; Wang et al., 2018). Herein, we report a portable spirometer based on triboelectric technology. It primarily consists of a small and light-weight breath-to-electrical (BTE) sensor (with a volume of 2.5 cm^3 and a weight of 1.8 g), a signal processing circuit, and a Bluetooth communication unit. When airflow is conducted into the mouthpiece, the BTE sensor is able to convert the breathing airflow into vibrations of the triboelectric membrane and thus generating the electrical signals. The frequency of the electrical current signals was chosen as the primary sensing parameter because of its linear relationship with airflow speed. The detectable flow rate of the BTE sensors can reach as low as 0.65 L/s (corresponding to an airflow speed of 1.3 m/s). Moreover, the sensor exhibits good stability (> 93%) under varying humidity conditions (from 35% to 81%). To effectively collect the electrical data and achieve wireless transmission, the circuit board is rationally designed to include a bridge rectifier, a micro-controller unit (MCU), and a Bluetooth chip, which greatly improves

the portability of the whole system. Furthermore, we developed an APP that is capable of displaying the pulmonary function parameters FVC, FEV_1, and FEV_1/FVC ratio in a user-friendly manner in real-time. The obtained results have a relative error of less than 3% in comparison to the commercial spirometer, demonstrating the practical potential of the wireless spirometer for point-of-care and home-based PFTs for rehabilitation care after COVID-19.

2. Results and discussion

2.1 Structure designs

The portable pulmonary function (PPF) monitor is primarily composed of a mouthpiece featuring an internal BTE sensor, a black surface enclosure (Fig. 1C), and a circuit module positioned in the lower part of the monitor that collects and transmits electrical signals (Fig. 1D, Fig. 1E, and Supplementary Video S1). The whole device has a volume of 233 cm^3 and a weight of 95.4 g, demonstrating its extremely high portability. As one exhaled into the mouthpiece, an alternating current was generated from the air flow induced membrane vibration, which was eventually collected via the circuit module. The following signal processing procedure includes three main steps. Firstly, the rectifier bridge transforms the alternating signals into direct current signals that are recognized by the analog-to-digital converter (ADC). Secondly, the ADC converts the analog signals into digital signals that can be transmitted wirelessly. Finally, when the Bluetooth low energy (BLE) module receives the digital signals, it will switch on and transmit the data to a mobile terminal. A flow diagram of the PPF monitor system is shown in Figure 1f.

The structure of the BTE sensor is schematically illustrated in Figure 1g. The device is principally composed of an acrylic framework, two aluminum (Al) plates forming an angle of 15°, and a polytetrafluoroethylene (PTFE) membrane that can flutter in between (Fig. 1H). Each lateral edge of the Al plates was chamfered into a wedge structure, acting as a wind guiding channel, as shown in Supplementary Figure S1. This design allows the PTFE membrane to flutter even at very low flow rates, down to 0.65 L/s (corresponding to the airflow speed of 1.3 m/s), resulting in electricity generation based on contact electrification and electrostatic induction (Zhu et al., 2012; Cui et al., 2020; Gong et al., 2020). The PTFE and Al were chosen as triboelectric materials due to their large different tendency to gain or lose electrons in contact electrification (Zou et al., 2019). PTFE micro/nanoparticles were sprayed onto both surfaces of the PTFE membrane as a nanoscale surface modification to enhance the effective friction area and hence the triboelectric effect (Zhu et al., 2013; Zhou et al., 2020; Chen et al., 2020; Chen et al., 2017). As shown in Figure 1i, the PTFE micro/nanoparticles were distributed densely and uniformly across the membrane which can greatly enhance the surface area of PTFE to increase the number of the surface tribo-charges. If micro/nanoparticles are sparse, the triboelectric effect will be weaken and the electric output will decrease significantly. The BTE sensor has a volume of 2.5 cm^3 (1.3 cm × 0.8 cm × 2.4 cm) and a weight of 1.8 g, which are 26 and 11 times, respectively, smaller than the sensor of a commercial spirometer (Contec SP10) (Supplementary Figure S2 and Supplementary Table S1). The small size of the BTE sensor allows it to be easily

installed inside the mouthpiece, acting as a self-powered airflow speed sensor for PPF monitoring in spirometry.

2.2 Working mechanism of breath-to-electrical (BTE) conversion

When airflow is exhaled into the mouthpiece and passes through the PTFE membrane, vortices are generated at the left and right end of the membrane, due to the Kármán vortex (Xu et al., 2017), forcing the PTFE to flutter periodically and contact alternatively with the two Al plates (Supplementary Figure S3 and Supplementary Video S2). After several periods of contact and separation, both sides of the PTFE membrane become negatively charged and the Al plates become positively charged, as a result of the triboelectric effect. When the PTFE membrane is in the middle stage of the device as shown in Fig. 2A(I), there is no potential difference between the two Al electrodes due to electrostatic equilibrium. If the PTFE membrane approaches one of the Al electrodes, such as the left electrode as shown in Fig. 2A(II), a current flows from right to left through an external load due to electrostatic induction (Zhou et al., 2020; Meng et al., 2020; Zhou et al., 2020; Jin et al., 2020; Zhou et al., 2020; Deng et al., 2020). When the PTFE membrane moves towards the right electrode (Fig. 2A(III)-(IV)), which is clearly revealed by the high-speed camera (Fig. 2B and Fig. 2C), a reverse current flows back from the left to the right electrodes. Therefore, cyclic electricity generation is accomplished with the respiration-induced fluttering of the PTFE membrane.

To obtain a quantitative understanding about the working mechanism, a three-dimensional COMSOL finite element simulation was employed to simulate the

electrical potential distributions between two electrodes under open-circuit conditions (Supplementary Figure S4 and Supplementary Video S3). A tribo-charge density of 3 nC/cm^2 was assumed on the surfaces of negatively-charged PTFE and positively-charged Al. The potential difference between two electrodes is defined as: $V_{OC} = U_L - U_R$, where V_{OC} is the open circuit voltage, with U_L and U_R being the electrical potentials of the left and right electrodes, respectively. The simulation covers the entire electricity generation cycle as discussed above, with the PTFE membrane first approaching the right electrode and then moving towards the left electrode. The simulated result of V_{OC} associated with the position of PTFE membrane is summarized in the Supplementary Figure S5.

A testing platform was designed and established to investigate the BTE signal conversion under different circumstances (Fig. 2D). To quantitatively characterize the conversion process, an air hose was employed to control the input airflow speed to the mouthpiece, and a commercial hot-wire anemometer recorded the airflow speed in real time. The whole measurement setup was then placed inside an acrylic box with a hydro-thermograph to monitor the temperature and humidity. With the above platform, the relationship between electrical outputs and airflow speeds were systemically studied. The temperature and the humidity inside the acrylic box during the test were 16.7 ℃ and 54.5%, respectively. Fig. 2E shows the results of transferred charge (Q_{SC}) between electrodes under short-circuit condition. As airflow speed increases from 2.9 m/s to 22.1 m/s, the peak Q_{SC} gradually increases from 0.9 nC to 3.2 nC, resulting from increasing contact areas as the PTFE membrane (with micro/nanoparticles on the

surface) collided intensively and closely with the Al plates at larger airflow speeds. However, when airflow speed is further increased, Q_{SC} remains almost unchanged due to the saturation of surface tribo-charges, as shown in Supplementary Figure S6a. A similar trend is observed in V_{OC} , as shown in Fig. 2F and Supplementary Figure S6b, which can be explained by the following classical equation of TENGs (Niu et al., 2013; Niu et al., 2013):

$$V_{OC} = Q_{SC}/C_{TENG} \quad (1)$$

where C_{TENG} is the device capacitance determined by the TENG structure, which remains constant during the experiment. For the short circuit current (I_{SC}), it increases with the airflow speed from 0.2 μA at 2.9 m/s to 4.5 μA at 22.1 m/s (Fig. 2G). Unlike the changing trend of Q_{SC} and V_{OC}, I_{SC} continues to increase to 6.2 μA with the airflow speed increasing to 24.5 m/s (Supplementary Figure S6c and S7). For TENG, I_{SC} is determined by the following equation:

$$I_{SC} = dQ_{SC}/dt \quad (2)$$

where t is the time. Hence, I_{SC} is determined by two aspects: the transfer of Q_{SC} and the transferred time. As the airflow speed begins to increase, both Q_{SC} and the fluctuating frequency of the PTFE membrane increase and contribute to increasing I_{SC}. After Q_{SC} reaches its saturated value, the oscillation frequency continues to grow with the airflow speed, leading to the continuous enhancement in I_{SC} (Supplementary Figure S8). According to the results discussed above, airflow speed is observed to affect Q_{SC}, V_{OC}, and I_{SC} in different ways, with both Q_{SC} and V_{OC} saturated at high speed, while I_{SC} does not reach any saturation. Therefore, I_{SC} is chosen as a key signal for sensing the breath airflow speed.

2.3 Performance of BTE sensor

Frequency and amplitude are the two main parameters of the I_{SC} signal, both of which were studied for sensing performance. The obvious nonlinear relationship between the current amplitude and the airflow speed is shown in Supplementary Figure S9. Moreover, large amplitude fluctuations at high speeds due to the irregular flutter of the PTFE membranes exacerbate the unreliability of sensing performance. The current frequency (f), on the other hand, exhibits a good linear relationship with the airflow speed (v) described by $f = 31.0v - 35.0$ ($R^2 = 0.981$) as shown in Fig. 3A. The linearity may be concluded from the equation of Strouhal number (Xu et al., 2017):

$$St = f_v l/v \tag{3}$$

where St is Strouhal number, f_v is the vortex-induced fluttering frequency, l is the length of the fluttering membrane, and v is the incoming airflow speed. Since St is approximately constant under the same test conditions, the frequency will be linearly correlated to the airflow speed. It is worth mentioning that changing l will affect the slope of the equation between f_v and v. More specifically, the smaller the length of the PTFE, the larger the slope will be.

Considering that human exhaled air contains large amounts of moisture, which then affects contact electrification, the electrical signals under different humidity conditions were further investigated. The humidity was controlled through a humidifier (whose outlet was connected into the acrylic box) with adjustable humidity levels, while the airflow speed was fixed at around 13 m/s. As shown in Fig. 3B, when the environmental humidity inside the acrylic box is adjusted from 35 % to 81 %, the current amplitude

decreases significantly by 25%, from about 0.8 μA to 0.6 μA. This indicates that the electrical outputs are apt to deteriorate under humid environments, due to the triboelectric effect being weakened. Nevertheless, the current frequency remains almost unchanged at about 361 Hz, regardless of humidity variation, exhibiting a stability greater than 93%. The current frequency depends on the cycle of the contact-separation of the PTFE membrane, which changes little with the humidity. Therefore, although the humidity reduces the current output of the TENG, the current frequency remains almost unchanged. Moreover, the stability investigation of the output performance was carried out for a period of 30 days. As shown in Fig. 3C, the current signal remained at almost 264 Hz under an airflow speed of 9.5 m/s. As a result, the current frequency with a higher linearity, stability, and resistance to humidity variation is chosen as the crucial sensing parameter. Comparative tests regarding sensing performance between the BTE sensor and the hot-wire anemometer under random airflow speeds are also shown in Fig. 3D. It was found that the airflow speed obtained from BTE sensor is consistent with that of a commercial device, indicating the reliability, accuracy, and feasibility of using the BTE sensor design as a core component for real-time breath airflow speed sensing.

2.4 Rehabilitation Care after COVID-19

Being able to calculate the flow-volume curve is an important function for a spirometer to evaluate pulmonary rehabilitation progress after COVID-19 treatment. The flow (F) and the volume (L) are determined by the following equations:

$$F = S \cdot v \tag{4}$$

$$L = \int F \cdot dt \tag{5}$$

where S is the cross-sectional area of airflow channel, v is the airflow speed derived from the current frequency of the BTE sensor, and t is the passing time of airflow.

Following the above discussion, we developed a PPF monitor based on the BTE sensor (Fig. 4A, Supplementary Figure S10 and Supplementary Video S4). The basic framework of the spirometry device is illustrated in Figure 4b. Firstly, a volunteer tester exhaled forcefully into the mouthpiece to drive the BTE sensor to generate an alternating analog signal. After the rectification of a full wave rectifier, the ADC module converts the analog signal into digital signals. Then, the MCU processes the digital signals and sends to the BLE for wireless transmission. At this stage, the digital signals are a list of magnitudes of currents. The detailed circuit diagrams are presented in Supplementary Figure S11. When a mobile terminal receives the data through Bluetooth connection with the PPF monitor, it starts to process the signal through a signal processing program which converts the magnitudes of current signals into frequency signal for the following operation. The flow chart of the program is specifically elaborated in Supplementary Figure S12, including noise filtering, frequency extraction, airflow speed calculations, volume integration, and result display. Concerning that the power line interference is always inevitable during our measurement, an algorithm program combining the output amplitude and frequency is developed to exclude the interference of noise signal. The logic of this algorithm program is filtering the noise signals through setting reasonable amplitude thresholds and operating sensing signals by contracting frequency values. The detailed process is

present in Supplementary Note S1. Using the above testing system, we performed actual PFTs on a volunteer. Firstly, we evaluated the normal status of the tester's pulmonary function as reference group. We also extracted information from the current signal (Supplementary Figure S13a) and converted it into the breath airflow speed (Supplementary Figure S13b), flow speed (Supplementary Figure S13c), volume (Supplementary Figure S13d), and then the flow-volume curve. As a result, the normal FVC value for the volunteer tester is 2.99 L, which could be directly obtained from the wireless spirometer (Fig. 4C). In addition, the FEV_1 value can be derived from the integration of the flow curve with respect to time for the initial time period of one second. It was calculated to be 2.12 L and the FEV_1/FVC ratio was found to be 71%, both of which are listed in Table 1 in detail. Afterwards, the volunteer tester conducted the second test (described as Stage 1) immediately after 15 minutes of vigorous exercise to simulate abnormal pulmonary function of COVID-19 patients (Custovic et al., 1994; Zavorsky et al., 2019). The results suggest that while FVC and FEV_1 decline significantly, FEV_1/FVC increases markedly compared to the reference group (Fig. 4D, Table 1, and Supplementary Figure S14), which is similar to the clinical feature of the discharged COVID-19 patients (Fumagalli et al., 2020). After a five-minute break, the tester took the third test (described as Stage 2) to simulate the rehabilitation of pulmonary function for COVID-19 patients. In this test, FVC and FEV_1 improved to some extent, but still failed to return to the reference group status (Fig. 4E, Table 1, and Supplementary Figure S15). About an hour later, the tester performed the last test to simulate recovered pulmonary function. It is evident that the indicators are almost

identical to the reference group, indicating a complete recovery of the pulmonary function (Fig. 4F, Table 1, and Supplementary Figure S16). The above tests demonstrate the feasibility of using this wireless spirometer to monitor the pulmonary rehabilitation process for discharged COVID-19 patients.

The effectiveness of the PPF monitor was further validated in the comparison tests, where a commercial spirometer (CONTEC SP10) was employed to record the forced expiratory flow-volume curves of each test from the same volunteer tester. Table 1 also presents the comparative results between the two spirometers. The relative error (% Err), defined as the value difference between the PPF monitor and the commercial spirometer, are all below 3% (Supplementary Table S2). These errors may have resulted from the following two aspects. First, the spirometers with different sensing principles may not have the same sensitivity. Second, some minor physiological state differences between the same volunteer tester may occur for different trials. However, it is important to note that the errors are within an acceptable range (Ambastha et al., 2016), especially for the FEV_1/FVC ratio, which fully demonstrates the clinical applicability of our PPF monitor for point-of-care PFTs.

It is worthwhile mentioning that spirometry is also of great significance for chronic obstructive pulmonary disease (COPD). COPD, characterized by airflow limitation or airway obstruction with respiratory symptoms such as chronic and progressive dyspnea (Choate et al., 2020; Mathers and Loncar, 2006), is becoming the fourth leading cause of death globally (Supplementary Figure S17). Although the disease is treatable at its early stage, it is largely under-diagnosed and under-treated, even when it becomes

clinically significant or enters moderately advanced stages (Choate and Mannino, 2017; Vogelmeier et al., 2017). The main criterion for diagnosing COPD is a FEV_1/FVC ratio of less than 70% (Cruz, 2007), which can be effectively and accurately diagnosed through spirometers. Additionally, spirometry is recommended once COPD is identified, and long-term monitoring is required to reduce morbidity or mortality in patients (Chung et al., 2020). From the aforementioned discussion, our PPF monitor is capable of providing crucial parameters, such as FEV_1, FVC, and their ratio, which are sufficient for the primary diagnosis and monitoring of COPD.

3. Conclusion

In summary, we propose a PPF monitor based on a triboelectric BTE sensor for evaluating the pulmonary function of COVID-19 patients. The BTE sensor is capable of generating substantial electrical signals without any external power supply through using the energy of airflow during respiration. It is apparent that the frequency of the current signals exemplifies a good linear relationship with airflow speed, with the sensor maintaining stable under differing humidity conditions as well. After data collection, the subsequent circuits can immediately convert the electrical signals and wirelessly transmit the data. Furthermore, a specialized program is able to analyze and display the pulmonary function parameters on the mobile terminal. Based on the aforementioned principles, a PPF monitor system with signal acquisition, signal processing, and wireless transmission modules was developed to monitor human pulmonary function in real time and provide critical evaluation parameters for pulmonary rehabilitation of COVID-19 patients. We expect that the PPF monitor

system will present a more convenient and low-cost approach than current commercial methods for rehabilitation care after the COVID-19.

4. Methods

4.1 Materials

PTFE membrane was purchased from DuPont. Aluminum foil (0.025mm thick, 99.45%) was purchased from Alfa Aesar. PTFE nanoparticle (Kontaflon 85) was purchased from Kontakt Chemie.

4.2 Fabrication of breath-to-electrical (BTE) sensor

The framework (acrylic) of BTE sensor was cut to a size of 13 mm, 8.0 mm, and 24 mm by a laser cutting machine (GY-D460C). Aluminum foils were attached on the inner surfaces of the framework whose edge sides have been chamfered into a wedge structure. A piece of PTFE membrane was placed at the middle of the framework. The BTE sensor was installed inside a commercial mouthpiece for the following tests.

4.3 Fabrication of wireless transmission module

The alternating signal generated by BTE sensor was converted into a DC signal through a commercial bridge rectifier (DB207s). A resistance (1 MΩ) was connected in parallel to divide the rectified voltage. A control chip (ATmega328) was selected to collect the electrical signal in real time through the analog port “A5”. The BLE module (HC-05) was connected to the “RXD” and “TXD” ports of the control chip. All the above components were soldered onto a circuit board.

4.4 Experimental setup for airflow speed tests

The mouthpiece with BTE sensor was placed inside a homemade testing platform (acrylic box). Airflow was generated from an air blower (Stanley STPT600) with speed control and guided to the BTE sensor through an air hose. An outlet of a humidifier was connected into the testing platform to adjust humidity. A hot wire anemometer (Smart sensor AR866A) was adopted to monitor the airflow speed in real time. The temperature and humidity are recorded by a hygrothermograph (Mijia).

4.5 Characterizations and Measurements

The surface of the PTFE membrane was characterized by scanning electron microscopy (Hitachi S5500). Both Q_{SC} and V_{OC} were measured by a Keithley 6514 electrometer (Tektronix). I_{SC} was measured by a SR570 current preamplifier (Stanford Research System). The fluttering behavior of the PTFE membrane in the BTE sensor was recorded using a high-speed camera (Revealer 5F01) at a frame rate of 2000 f/s.

4.6 Experimental setup for pulmonary function tests

Volunteer testers exhaled into the wireless PPF monitor for pulmonary function tests. A commercial spirometer (Contec SP10) was employed to monitor pulmonary function parameters with the same process for comparison. The volunteer testers participating in PFTs are also co-authors of this manuscript. All participants have confirmed the details of the experiment and no ethical approval was required in this case.

Author Contributions

L.W., J.C. and Y.X. guided the whole project. L.W., J.C., Y.X., Q.X., Y.F, Q.J. and N.H. conceived the idea, designed the experiment, analyzed the data, drew the figures, and composed the manuscript. All authors made technical comments on the manuscript.

The manuscript was written through contributions of all authors. All authors have given the approval to the final version of the manuscript. The volunteers participating in the PFTs are also co-authors of this manuscript. J.C. submitted the manuscript and was the lead contact. All authors have seen the paper, agree to its content, and approve submission.

Declaration of competing interest

Patents have been filed to protect the reported technologies. The authors declare no other competing interests.

Acknowledgments

L. W. and Y. X. acknowledges the National Natural Science Foundation of China (Nos. 61601394, 61974071), National Key Research and Development Program of China (2017YFA0205302), Priority Academic Program Development of Jiangsu Higher Education Institutions (PAPD, YX030003), Jiangsu Provincial Key Research and Development Program (BE2018732), Jiangsu Shuangchuang Talent Program, the Science and Technology Innovation Project for Overseas Students in Nanjing, Start-Up Fund from Nanjing University of Posts and Telecommunications (No. NY218151 and NY218157). J. C. acknowledges the Henry Samueli School of Engineering & Applied Science and the Department of Bioengineering at the University of California, Los Angeles for the startup support. J.C. also acknowledges the 2020 Okawa Foundation Research Grant.

References

Ambastha, S., Umesh, S., Maheshwari K, U., Asokan, S., 2016. *J. Lightwave Technol. 34*, 5682-5688.

Chen, G., Li, Y., Bick, M., Chen, J., 2020. *Chem. Rev. 120*, 3668-3720.

Chen, J., Wang, Z. L, 2017 *Joule 1*, 480-521.

Choate, R., Mannino, D. M, 2017. *JCOM 24*, 172-180.

Choate, R., Pasquale, C. B., Parada, N. A., Prieto-Centurion, V., Mularski, R. A., Yawn, B. P., 2020. *Chronic Obstr. Pulm. Dis. 7*, 49-59.

Chung, H., Jeong, C., Luhach, A. K., Nam, Y., Lee, J., 2019. *Evol. Bioinf. Online 15*, 1-8.

Cruz, A. A. Global Surveillance, Prevention and Control of Chronic Respiratory Diseases- a Comprehensive Approach. *World Health Organization*, 2007.

Custovic, A., Arifhodzic, N., Robinson, A., Woodcock, A., 1994. *Chest 105*, 1127-1132.

Deng, W., Zhou, Y., Zhao, X., Zhang, S., Zou, Y., Xu, J., Yeh, M. H., Guo, H., Chen, J., 2020. *ACS Nano 14*, 9050-9058.

Dirksen, A., Holstein-Rathlou, N. H., Madsen, F., Skovgaard, L. T., Ulrik, C. S., Heckscher, T., Kok-Jensen, A., 1998. *J. Appl. Physiol. 85*, 259-265.

Fajnzylber, J., Regan, J., Coxen, K., Corry, H., Wong, C., Rosenthal, A., Worrall, D., Giguel, F., Piechocka-Trocha, A., Atyeo, C., Fischinger, S., Chan, A., Flaherty, K. T., Hall, K., Dougan, M., Ryan, E. T., Gillespie, E., Chishti, R., Li, Y., Jilg, N.,

Hanidziar, D., Baron, R. M., Baden, L., Tsibris, A. M., Armstrong, K. A., Kuritzkes, D. R., Alter G., Walker, B. D., Yu, X., Li, J. Z., 2020. *Nat. Commun. 11*, 5493.

Fan, F.-R., Tian, Z.-Q., Lin Wang, Z., 2012. *Nano Energy 1*, 328-334.

Fumagalli, A., Misuraca, C., Bianchi, A., Borsa, N., Limonta, S., Maggiolini, S., Bonardi, D. R., Corsonello, A., Di Rosa, M., Soraci, L., Lattanzio, F., Colombo, D., 2020. *Infection 49*, 153-157.

Gong, H., Xu, Z., Yang, Y., Xu, Q., Li, X., Cheng, X., Huang, Y., Zhang, F., Zhao, J., Li, S., Liu, X., Huang, Q., Guo, W., 2020. *Biosens. Bioelectron. 169*, 112567.

Graham, B. L., Steenbruggen, I., Miller, M. R., Barjaktarevic, I. Z., Cooper, B. G., Hall, G. L., Hallstrand, T. S., Kaminsky, D. A., McCarthy, K., McCormack, M. C., Oropez, C. E., Rosenfeld, M., Stanojevic, S., Swanney, M. P., Thompson, B. R., 2019. *Am. J. Respir. Crit. Care Med. 200*, e70-e88.

Guo, H., Pu, X., Chen, J., Meng, Y., Yeh, M.-H., Liu, G., Tang, Q., Chen, B., Liu, D., Qi, S., Wu, C., Hu, C., Wang, J., Wang, Z. L., 2018. *Sci. Robot. 3*, eaat2516.

Jiang, D., Shi, B., Ouyang, H., Fan, Y., Wang, Z. L, Li, Z., 2020. *ACS Nano* 14, 6436-6448.

Jin, L., Xiao, X., Deng, W., Nashalian, A., He, D., Raveendran, V., Yan, C., Su, H., Chu, X., Yang, T., Li, W., Yang, W., Chen, J., 2020. *Nano Lett. 20*, 6404-6411.

Kouri, A., Gupta, S., Yadollahi, A., Ryan, C. M., Gershon, A. S., To, T., Tarlo, S. M., Goldstein, R. S., Chapman, K. R., Chow, C. W., 2020. *Chest 158*, 2502-2510.

Leocadio, R. R. V., Segundo, A. K. R., Louzada, C. F., 2019. *Sensors 19*, 5095-5112.

Lu, Y., Lou, Z., Jiang, K., Chen, D., Shen, G., 2019. *Mater. Today Nano 8,* 100050.

Mathers, C. D., Loncar, D., 2006. *PLoS Med. 3*, e442.

Meng, K., Zhao, S., Zhou, Y., Wu, Y., Zhang, S., He, Q., Wang, X., Zhou, Z., Fan, W., Tan, X., Yang, J., Chen, J., 2020. *Matter 2*, 896-907.

Niu, S., Liu, Y., Wang, S., Lin, L., Zhou, Y. S., Hu, Y., Wang, Z. L., 2013. *Adv. Mater. 25*, 6184-6193.

Niu, S., Wang, S., Lin, L., Liu, Y., Zhou, Y. S., Hu, Y., Wang, Z. L., 2013 *Energy Environ. Sci. 6*, 3576-3583.

Pu, X., Guo, H., Chen, J., Wang, X., Xi, Y., Hu, C., Wang, Z. L., 2017. *Sci. Adv. 3*, e1700694.

Su, Y., Wang, J.., Wang, B., Yang, T., Yang, B., Xie, G., Zhou, Y., Zhang, S., Tai, H., Cai, Z., Chen G., Jiang, Y., Chen, L.-Q., Chen, J., 2020. *ACS Nano* 14, 6067-6075.

Vogelmeier, C. F., Criner, G. J., Martinez, F. J., Anzueto, A., Barnes, P. J., Bourbeau, J., Celli, B. R., Chen, R., Decramer, M., Fabbri, L. M., Frith, P., Halpin, D. M., Lopez Varela, M. V., Nishimura, M., Roche, N., Rodriguez-Roisin, R., Sin, D. D., Singh, D., Stockley, R., Vestbo, J., Wedzicha, J. A., Agusti A., 2017. *Am. J. Respir. Crit. Care Med. 195*, 557-582.

Wang, M., Zhang, J., Tang, Y., Li, J., Zhang, B., Liang, E., Mao, Y., Wang, X., 2018. *ACS Nano 12,* 6156-6162.

Wang, S., Lin, L., Wang, Z. L., 2015. *Nano Energy 11*, 436-462.

Wang, Z. L., 2014 *Faraday Discuss. 176*, 447-458.

West, T., Theron, A., 2015. *Intensive Care Med. 16*, 114-118.

Xu, M., Wang, Y.-C., Zhang, S. L., Ding, W., Cheng, J., He, X., Zhang, P., Wang, Z., Pan, X., Wang, Z. L., 2017. *Extreme Mech. Lett. 15*, 122-129.

You, J., Zhang, L., Ni-Jia-Ti, M. Y., Zhang, J., Hu, F., Chen, L., Dong, Y., Yang, K., Zhang, B., Zhang, S., 2020. *J. Infect. 81*, e150-e152.

Zavorsky, G. S., Zimmerman, R. D., Shendell, D. G., Goodfellow, L. T., 2019. *Respir. Care 64*, 26-33.

Zhao, D., Yao, F., Wang, L., Zheng, L., Gao, Y., Ye, J., Guo, F., Zhao, H., Gao, R., 2020. *Clin. Infect. Dis. 71*, 756-761.

Zhou, P., Yang, L., Huang, Y. X., 2019. *Sensors 19*, 2487-2497.

Zhou, Y., Deng, W., Xu, J., Chen, J., 2020. *Cell Rep. Phys. Sci. 1*, 100142.

Zhou, Z., Chen, K., Li, X., Zhang, S., Wu, Y., Zhou, Y., Meng, K., Sun, C., He, Q., Fan, W., Fan, E., Lin, Z., Tan, X., Deng, W., Yang, J., Chen, J., 2020. *Nat. Electron. 3*, 571-578.

Zhou, Z., Padgett, S., Cai, Z., Conta, G., Wu, Y., He, Q., Zhang, S., Sun, C., Liu, J., Fan, E., Meng, K., Lin, Z., Uy, C., Yang, J., Chen, J., 2020. *Biosens. Bioelectron. 155*, 112064.

Zhou, Z., Weng, L., Tat, T., Libanori, A., Lin, Z., Ge, L., Yang, J., Chen, J., 2020. *ACS Nano 14*, 14126-14133.

Zhu, G., Lin, Z. H., Jing, Q., Bai, P., Pan, C., Yang, Y., Zhou, Y., Wang, Z. L., 2013. *Nano Lett. 13*, 847-853.

Zhu, G., Pan, C., Guo, W., Chen, C. Y., Zhou, Y., Yu, R., Wang, Z. L., 2012. *Nano Lett. 12*, 4960-4965.

Zou, H., Zhang, Y., Guo, L., Wang, P., He, X., Dai, G., Zheng, H., Chen, C., Wang, A. C., Xu, C., Wang, Z. L., 2019. *Nat. Commun. 10*, 1427.

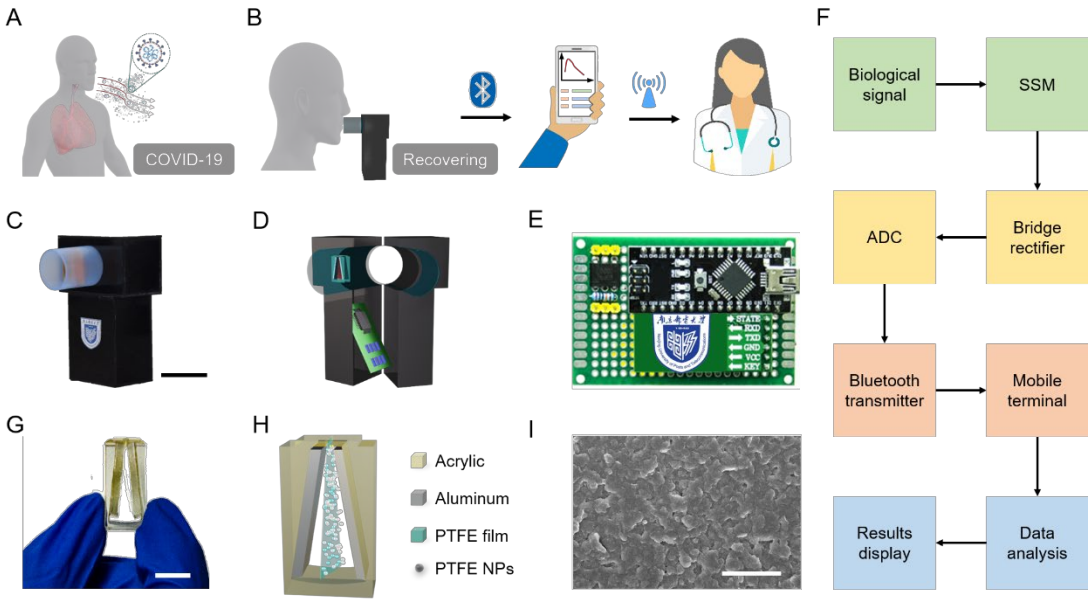

Fig. 1. Schematic illustrations of the wireless spirometer. (A) Diagram of a patient suffering from COVID-19. (B) An ideal approach to monitor the patient's pulmonary function through a wireless spirometer. (C) Photograph and (D) vertical section of our proposed PPF monitor based on a BTE sensor. Scale bar, 5 cm. (E) Photograph of the circuit module including a signal processing circuit and a Bluetooth communication unit. (F) Process flow chart of our PPF monitoring system, displaying the paths from signal acquisition (green), signal processing (yellow), wireless transmission (light red) to data analysis and results display (blue) through a mobile terminal (along the arrowhead direction). (G) Photograph and (H) diagram of the BTE sensor. Scale bar, 1 cm. (I) SEM image of the PTFE micro/nanoparticles sprayed onto both surfaces of the PTFE membrane. Scale bar, 10 μm.

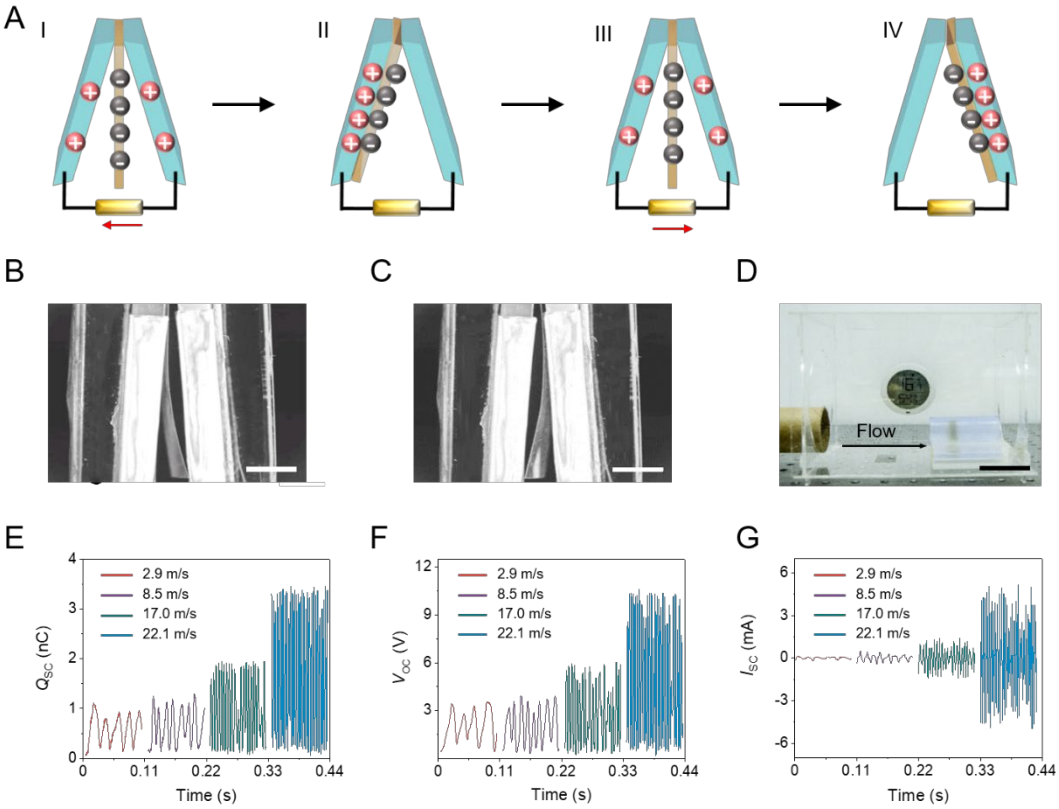

Fig. 2. Working mechanism and electrical outputs of BTE Sensor. (A) Working mechanism of the BTE sensor. (B), (C) Vibration patterns of the PTFE membrane at different positions. Scale bar, 3 mm. (D) Photograph of a testing platform for investigate the electrical signals of the BTE sensor under different conditions. Scale bar, 5 cm. (E) Q_{SC}, (F) V_{OC} and (G) I_{SC} of the BTE sensor at varying airflow speeds.

.

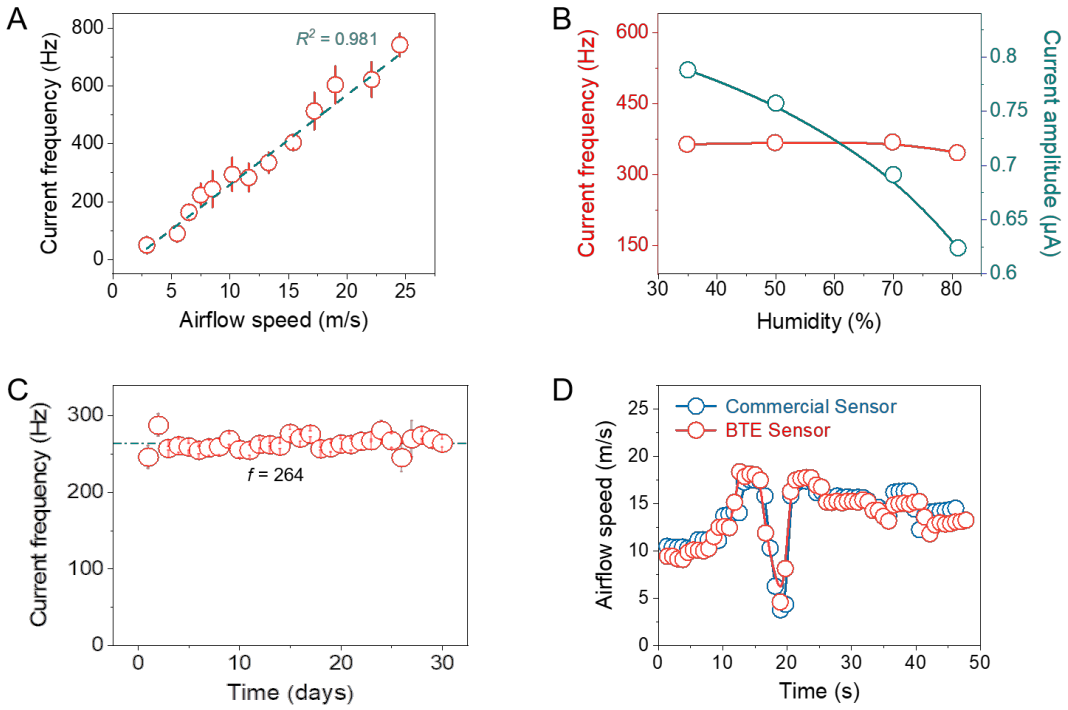

Fig. 3. Performance of the BTE sensing module. (A) Relationship between current frequency and airflow speed (R^2 = 0.981). (B) Current frequency and amplitude of the BTE sensor under different ambient humidity (from 35% to 81%) at an airflow speed of 13 m/s. (C) Stability of the BTE sensor at an airflow speed of 9.5 m/s. (D) Results of a comparative test about the sensing performance between the BTE sensor and a hot-wire anemometer under random airflow speeds.

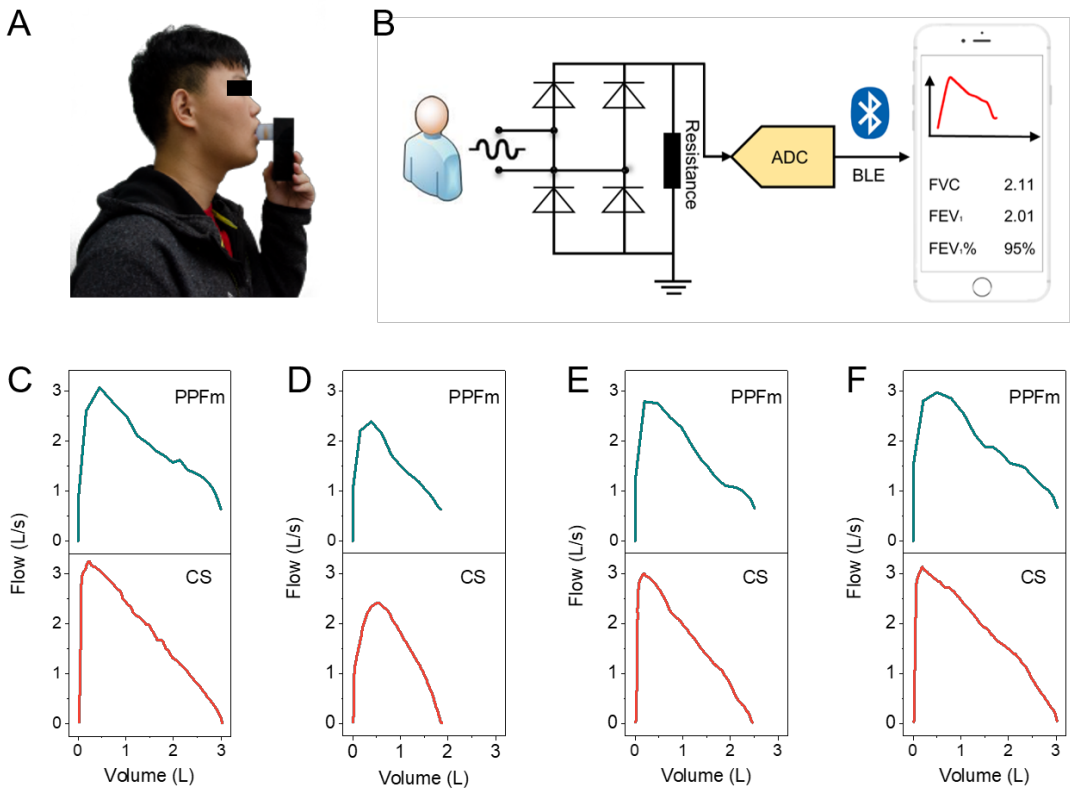

Fig. 4. Demonstration of the wireless spirometer. (A) Photograph of the pulmonary function test using our wireless PPF monitor for a volunteer tester. (B) Flow diagram of the test process and the visualization of the test results. (C), (D), (E), (F) Results of PFTs at four different stages: reference group, Stage 1, Stage 2, and recovered group, respectively. The upper parts are the results of our PPF monitor and the lower parts are the comparison charts of a commercial spirometer.

Table 1. Comparative results obtained from CS (commercial spirometer) and PPFm (portable pulmonary function monitor).

Tester	FVC (L)		FEV_1 (L)		FEV_1/FVC (%)	
	CS	PPFm	CS	PPFm	CS	PPFm
Normal	3.05	2.99	2.15	2.12	70	71
Stage 1	1.88	1.85	1.63	1.59	87	86
Stage 2	2.47	2.50	1.88	1.90	76	75
Recovered	3.01	3.02	2.17	2.18	72	72